



**HAL**  
open science

## **22 W average power multiterawatt femtosecond laser chain enabling 1019 W/cm<sup>2</sup> at 100 Hz**

R. Clady, Y Azamoum, L Charmasson, A Ferré, O Utéza, M Sentis

► **To cite this version:**

R. Clady, Y Azamoum, L Charmasson, A Ferré, O Utéza, et al.. 22 W average power multiterawatt femtosecond laser chain enabling 1019 W/cm<sup>2</sup> at 100 Hz. Applied Physics B - Laser and Optics, 2018, 124 (5), 10.1007/s00340-018-6958-1 . hal-02137921

**HAL Id: hal-02137921**

**<https://amu.hal.science/hal-02137921>**

Submitted on 23 May 2019

**HAL** is a multi-disciplinary open access archive for the deposit and dissemination of scientific research documents, whether they are published or not. The documents may come from teaching and research institutions in France or abroad, or from public or private research centers.

L'archive ouverte pluridisciplinaire **HAL**, est destinée au dépôt et à la diffusion de documents scientifiques de niveau recherche, publiés ou non, émanant des établissements d'enseignement et de recherche français ou étrangers, des laboratoires publics ou privés.

# 22 W average power multiterawatt femtosecond laser chain enabling $10^{19}$ W/cm<sup>2</sup> at 100 Hz

R. Clady<sup>1</sup> · Y. Azamoum<sup>1</sup> · L. Charmasson<sup>1</sup> · A. Ferré<sup>1</sup> · O. Utéza<sup>1</sup> · M. Sentis<sup>1</sup>

Received: 12 January 2018 / Accepted: 21 April 2018  
© Springer-Verlag GmbH Germany, part of Springer Nature 2018

## Abstract

We measure the wavefront distortions of a high peak power ultrashort (23 fs) laser system under high average power load. After 6 min—100 Hz operation of the laser at full average power (> 22 W after compression), the thermally induced wavefront distortions reach a steady state and the far-field profile of the laser beam no longer changes. By means of a deformable mirror located after the vacuum compressor, we apply a static pre-compensation to correct those aberrations allowing us to demonstrate a dramatic improvement of the far-field profile at 100 Hz with the reduction of the residual wavefront distortions below  $\lambda/16$  before focusing. The applied technique provides 100 Hz operation of the femtosecond laser chain with stable pulse characteristics, corresponding to peak intensity above  $10^{19}$  W/cm<sup>2</sup> and average power of 19 W on target, which enables the study of relativistic optics at high repetition rate using a moderate  $f$ -number focusing optics ( $f/4.5$ ).

## 1 Introduction

Over the past decades, the rapid progress in generating laser pulses with high peak power enabling peak intensities in excess of  $10^{18}$  W/cm<sup>2</sup> has opened up a new field of physics. Such laser pulses are used for various applications, such as high energy physics or the production of highly energetic particles and photons. In particular, laser-driven electrons [1], ion-acceleration [2] and the generation of X-ray via laser-plasma interaction [3] are currently under intense investigation as these laser-induced secondary sources could enable easy access to low cost, table-top particle accelerator and radiation generator devices. Nevertheless, the relatively low conversion efficiency of these processes limits the radiant intensity of the laser-induced secondary sources. Its enhancement requires the development of laser systems with sufficiently high peak power (> TW) to efficiently generate them and the access to high repetition rate (> 10 Hz) to increase their average flux in view of the development of applications. However, some technological issues impede to produce high peak power lasers and simultaneously high repetition rate lasers [4]. The management of the thermal load within the laser is the main difficulty for

high repetition rate laser [5] while the main challenge in the case of high peak power lasers is to manage the optical nonlinearities inherent to the propagation of high peak power pulses through optical media. Current developments tend to reach high peak power at high repetition rate by reducing the pulse duration (few cycle pulses) using, for instance, hollow fiber compressor devices but the pulse energy remains modest (< 10 mJ per pulse) [6–8]. Reaching high peak power and high average power simultaneously can be obtained using complex architecture, such as coherent combination [9], pulse stacking [10] or divided pulse amplification [11]. One of the most promising routes to the generation of high peak power and high repetition rate simultaneously is based on OPCPA technology driven by TW-scale pump pulses from Ytterbium-based laser at kW scale average power [12, 13]. Indeed, the management and the control of thermally induced wavefront distortions have been intensively studied not only in Yb:YAG amplifier systems [14–16] but also in different amplifier media such as Nd:glass [17] or Ti:Sa [18–20]. These technologies are now mature and high average power ranging from tens to hundreds of watts recently became available from diode-pumped fiber, slab and cryogenically cooled thin disk lasers [4] allowing to scale OPCPA-based laser systems towards combined high peak power (> 5 TW) and high average power (> 50 W) performances [12].

However, for CPA-based femtosecond laser machines implying the delivery of high average and high peak power

---

✉ R. Clady  
clady@lp3.univ-mrs.fr

<sup>1</sup> Aix Marseille Université, CNRS, LP3 UMR 7341,  
13288 Marseille, France

on target, the high thermal load needs to be managed not only along the laser chain, but also along the beam transport until the target. Indeed, thermally induced phase aberrations degrade the wavefront of the laser pulses and affect the overall laser performances [21]. Only few studies devoted to the management of thermal effects during the beam transport (after amplification) can be found. They mostly deal with the management of thermal effects taking place in the compressor of high average power CPA laser chains [22–24]. Indeed, the laser energy absorption and subsequent heat removal from diffraction gratings in CPA compressors is challenging in the context of the development of high repetition rate, high peak power laser systems. Active cooling of diffraction gratings [25] is considered to solve this issue but this technique is complex and costly. Bulk compressors and down-chirped amplification [12, 26] are alternative strategies to avoid the use of metallic gratings. However, they have been so far limited to modest pulse energy (< 100 mJ) because of the high accumulated B-integral. For high average power (> 10 W) high energy (> 100 mJ per pulse) femto-second CPA lasers, it has been shown that thermally-related wavefront distortions are mainly composed of low frequency aberrations, such as defocus [23]. A straightforward way to manage those phase aberrations is to compensate them using adaptive optics.

In this article, we present experimental results of the characterization of a laser system combining unique performances: a peak power above 9.5 TW, a high repetition rate (100 Hz), a high average power (32 W before compression, 22 W after compression) and an ASE contrast ratio around  $10^{10}$ . We investigate the wavefront distortions induced by the high thermal load on optical components located in vacuum

after the power amplifier. We find that our adaptive optic system can not only compensate for the static wavefront distortions accumulated along the laser chain, but also for most of the thermally-induced wavefront distortions, which are significant for average power higher than 10 W. After compensation of the wavefront aberrations, we demonstrate the delivery of a stable 100 Hz train of pulses with an average power of 19 W on target and peak intensity higher than  $10^{19}$  W/cm<sup>2</sup> using a moderate  $f$ -number ( $f/4.5$ ) parabolic mirror.

## 2 Laser system description

A schematic figure of the laser system is shown in Fig. 1. The system is a commercial prototype built by Amplitude Technologies based on Ti:Sa technology and CPA architecture. A preamplifier, pumped by a 100 Hz diode-pumped frequency-doubled (532 nm) Nd:YAG laser (Centurion from Quantel, 20 mJ) and incorporating a saturable absorber (SA) and 100 Hz pulse picker, is inserted between the oscillator and the stretcher. This configuration provides clean high-energy ( $\sim 10$   $\mu$ J) seed-pulse injection in the regenerative amplifier [27] and allows keeping the amplified spontaneous emission (ASE) level as low as possible. The cleaned seed pulse is then stretched up to about 600 ps FWHM in an Öffner type stretcher [28]. In order to pre-compensate for the modifications of the spectral amplitude induced by amplification but also for the modification of the spectral phase due to the propagation in dispersive element along the laser chain, a combination of a high-resolution acousto-optic programmable dispersive filter (DAZZLER from Fastlite)

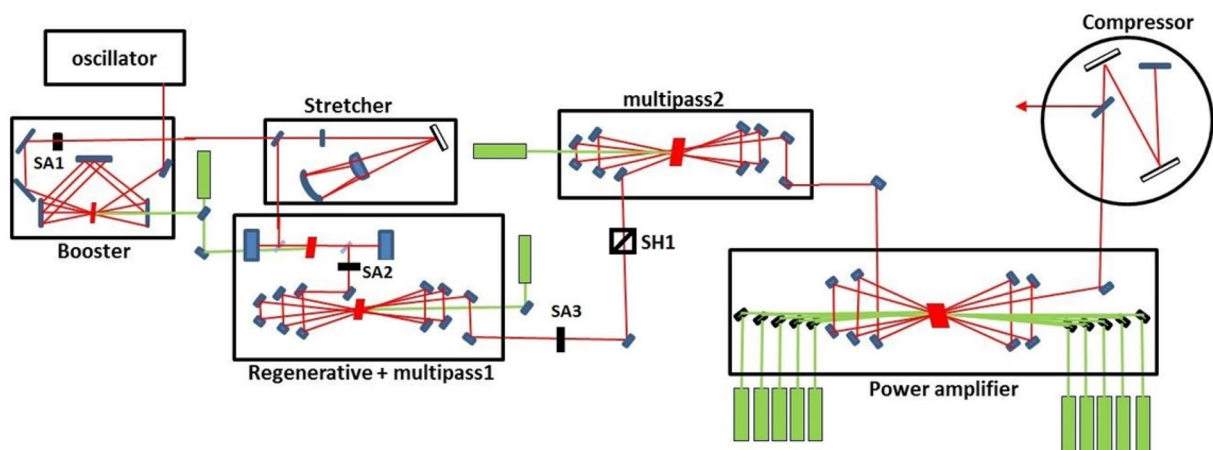


**Fig. 1** The 100 Hz multi-TW laser set-up. SA1, SA2 and SA3 are saturable absorbers (RG-850 long pass filters, 2 mm thick for SA1, 1 mm thick for SA2 and SA3), SH1 is an electronic fast shutter (Newport, model 76992) whose aperture diameter is 6 mm, with an opening time < 1 ms. The pulse energy is measured at 10  $\mu$ J after the

Booster, at 0.7 mJ after the regenerative amplifier, at 5 mJ after the multipass1 and at 25 mJ after multipass2. It should be mentioned that a set of beam splitters (not shown in Fig. 1) is inserted after multipass1 and only 1 mJ is sent into the multipass2

[29] and of an acousto-optic programmable gain control filter (MAZZLER from Fastlite) [30] is used in the laser chain. The Dazzler is inserted after the Öffner stretcher and enables to control the spectral phase of the pulse. The Mazzler is inserted inside the regenerative cavity to compensate for the red-shift induced by the amplification, the spectral gain narrowing and the red-shift induced by the saturable absorbers located along the laser chain. A Pockels cell (3 ns rise time) and a Brewster polarizer are placed just after the regenerative amplifier to filter pre-pulses in the ns range. Two successive 5-pass multipass amplifiers pumped by 100 Hz diode-pumped frequency-doubled (532 nm) Nd:YAG lasers (Centurion from Quantel-20 mJ and DPSS250 from Innolas-100 mJ) produce a 100 Hz pulse train with 25 mJ pulse energy before the final power amplifier. To further increase the laser-intensity contrast ratio, we insert two other similar SA in the laser chain. The beam is transmitted through the first SA after the regenerative cavity with an incident fluence around  $15 \text{ mJ/cm}^2$ . After the first multipass amplifier, the beam is transmitted through the second SA with an incident fluence around  $30 \text{ mJ/cm}^2$ . The beam transmission coefficient is around 70% for each SA.

The last 100 Hz amplifier is pumped by ten 100 Hz flashlamp-pumped frequency doubled (532 nm) Nd:YAG lasers (Nano-TRL 250 by Litron) delivering 100 mJ each, as described in Fig. 1. To avoid the thermally induced spatial distortions produced by the high average pump power (100 W), the Ti:Sa crystal is housed in a cryogenic chamber and cooled down at a temperature of 100 K to improve the evacuation of the residual heat related to the pumping power and to reduce both the refractive index gradient and the thermo-mechanical stress [31].

Pulses are amplified up to 324 mJ at 100 Hz with an energy stability of 0.9% rms, as shown in Fig. 2a. The pulse energy can be continuously adjusted before the compressor without any change in the temporal and spatial beam profile by the use of a half-waveplate and two Brewster polarizers.

According this mode of operation, the laser chain is run at full power (32 W) until the attenuation system located just before the compressor chamber. The transmission coefficient of the vacuum compressor was measured at 69% with low pulse energy (30 mJ) and at atmospheric pressure. This coefficient is considered in first approximation independent of the incoming pulse energy. The maximum pulse energy after compression is, therefore,  $\sim 220 \text{ mJ}$ . Figure 2b shows the spectral amplitude and phase measured after compression using self-reference spectral interferometry (Wizzler, Fastlite) [32] and Fig. 2c shows the resulting pulse temporal profile, with a pulse duration of 23 fs (FWHM). Considering the measured energy and pulse duration, the pulse peak power is higher than 9.5 TW at 100 Hz repetition rate, with an average power greater than 22 W. After compression, the collimated beam has a beam diameter of  $\sim 33 \text{ mm}$  at  $1/e^2$ .

The pulse temporal contrast has been analyzed in the nanosecond time range with a fast photodiode (150 ps rise time) coupled to a 3.5-GHz oscilloscope and a set of calibrated neutral density filters at 800 nm, in a similar manner we did on our 10 Hz–20 TW laser system [33]. We observed pre-pulses at 15, 9.8 and 5 ns before the main pulse. The pre-pulse at  $-9.8 \text{ ns}$  is generated inside the regenerative amplifier by the leakage of the polarizer/Pockels cell combination. The two other pre-pulses at  $-5$  and  $-15 \text{ ns}$  are not detected before the final power amplifier. They are presumably due to laser beam scattering on the Ti:Sa crystal or mirrors during the power amplification stage [34]. All these ns pre-pulses have a temporal contrast higher than  $5 \times 10^7$ . Considering a target having an ionization threshold around  $10^{12} \text{ W/cm}^2$ , none of these pre-pulses will affect the latter as long as the main pulse peak intensity is not higher than  $5 \times 10^{19} \text{ W/cm}^2$ .

The pulse temporal contrast was measured on a time scale up to 0.5 ns using a third-order autocorrelator from Amplitude Technologies (Sequoia). Figure 3 shows the normalized intensity profile of the laser for time delay ranging from  $-480 \text{ ps}$  to the main pulse. At  $-480 \text{ ps}$ , the

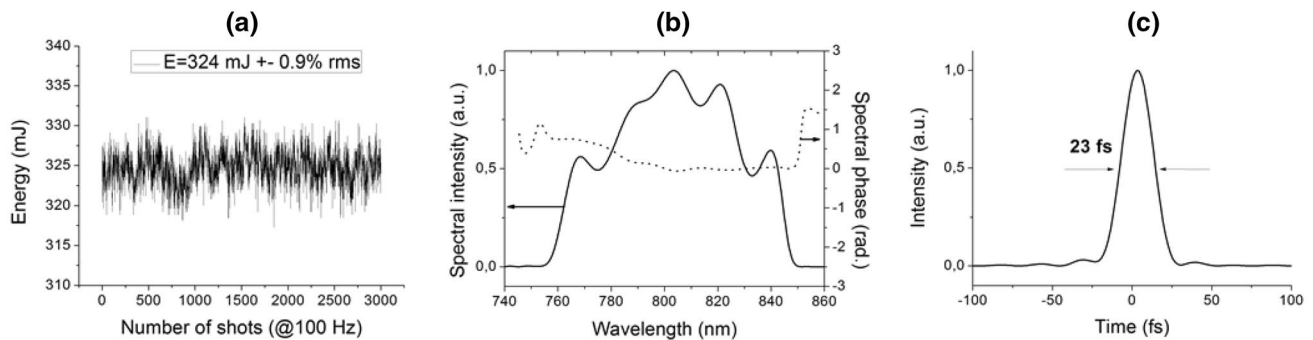


**Fig. 2** **a** Evolution of the pulse energy before compression. The average energy is  $\sim 324 \text{ mJ}$  per pulse with an energy stability of 0.9% rms. **b** Spectral intensity (solid lines) and phase (dot line) of the amplified

compressed beam, measured by self-referenced spectral interferometry and **c** temporal intensity profile

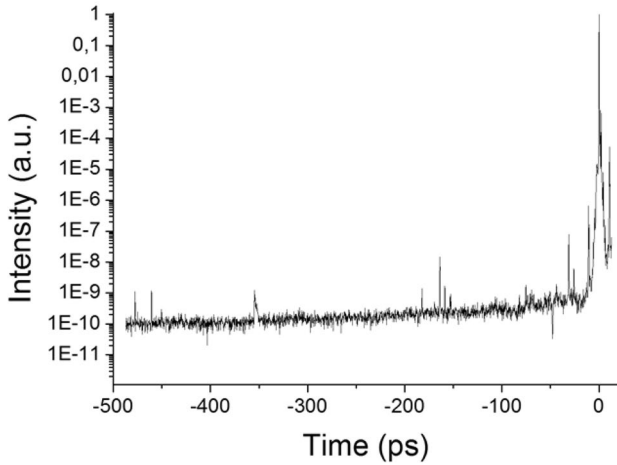


**Fig. 3** Third order autocorrelation trace of the amplified pulse for delay up to 480 ps before the main pulse. The dip near  $-50$  ps shows the actual noise level of this measurement

ASE intensity contrast ratio, defined as the ratio between the main peak intensity and the ASE intensity, is measured at  $10^{10}$ . A slight increase of the ASE pedestal level is observed from  $-480$  to  $-50$  ps while one would expect a flat ASE temporal profile in this temporal time scale. This is due to the two SA (SA2 and SA3) which are inserted in the laser chain before the compressor, where the laser pulse is chirped ( $\sim 600$  ps FWHM) and temporally overlapped with the ASE. The absorption of each SA is progressively saturated by the stretched pulse. As a consequence, the ASE absorption decreases progressively when approaching the main pulse.

We also note that because of the limited spectral acceptance of the non-linear crystals used in the autocorrelator, the intensity of the main pulse is underestimated by a factor  $\sim 5$  with respect to the ASE intensity. Therefore, the ASE intensity contrast ratio is underestimated by the same factor.

Regarding the peaks positioned at short picosecond time-scale on the ASE pedestal, we believe that the pre-pulses beyond  $-10$  ps are artifacts induced by our third-order autocorrelator (Sequoia) as a slight change of the Sequoia alignment induces a change in the temporal position of those peaks. They are, therefore, likely to be induced by scattering of the pulse on the numerous optics of the Sequoia. However, it is conceivable that the pre-pulse at  $-10$  ps is a real pre-pulse which would be generated in the different amplification stages by energy transfer from an initial post-pulse (generated by the 1 mm thick SA) [35, 36]. Further studies are necessary to conclude about the nature (pre/post) of this pulse, which could be eliminated, if needed, using post-compression contrast enhancement technique, like double plasma mirror for instance [37].

### 3 Thermally induced aberrations: characterization and management

Figure 4 shows the experimental set-up for high-intensity experiments comprising diagnostics and optical devices for control and management of the laser beam properties. After the attenuation stage and the Treacy type compressor, the beam is directed in a vacuum chamber where an adaptive optic system (ILAO, Imagine Optic [38]) is used to correct for the wavefront aberrations of the amplified compressed beam. In this chamber, the beam is reflected by a set of large bandwidth dielectric mirrors and a deformable mirror (DM) with a protected silver coating. To measure the wavefront, the beam on the DM is image relayed onto a Shack–Hartmann wavefront sensor (WFS) from the leak of a high reflectivity mirror located after the DM. The beam is then propagated into the interaction chamber where the beam is focused by a  $f/4.5$  off-axis parabolic mirror (OAP). In order to measure the beam spatial profile in the focal plane even at the maximum pulse energy, we install two parallel planar optical uncoated substrates (Ws) at  $45^\circ$  incident angle to redirect the reflected beam for spatial characterization. The laser focal spot is then image relayed by an achromatic doublet lens on the surface of a CCD camera with a magnification factor of 8.6.

We first run the laser chain at low compressed energy (30 mJ – 3W). In this operating condition, the adaptive optics loop correction system allows us to compensate for the low frequency wavefront distortions accumulated along the laser chain. The beam radius at the focal plane (averaged along the two orthogonal axes) is measured at  $5.2 \mu\text{m}$  ( $1/e^2$ ). This adjustment of the deformable mirror defines the reference wavefront which allows us to get the focused spot of the highest quality in the focal plane of the parabola. This strategy takes into account all the aberrations of the laser chain and of the optics positioned until the plane in which the high-intensity applications are developed [36].

In order to evaluate the importance of the wavefront distortions at the maximum energy capability of the laser system [ $\sim 320$  mJ (32W) before compressor], we study the differential wavefront distortions corresponding to the subtraction of the actual measured wavefront to the wavefront reference which was determined beforehand when the laser was attenuated to a low average power (3 W). The evolution of the wavefront aberrations as a function of time upon opening the shutter SH1 is shown in Fig. 5 by fitting the measured wavefront with orthonormal Zernike polynomials [39]. We consider the time-dependent evolution of the following low-order Zernike modes [40]: defocus, astigmatism ( $0^\circ$  and  $45^\circ$ ) and coma ( $0^\circ$  and  $90^\circ$ ). They

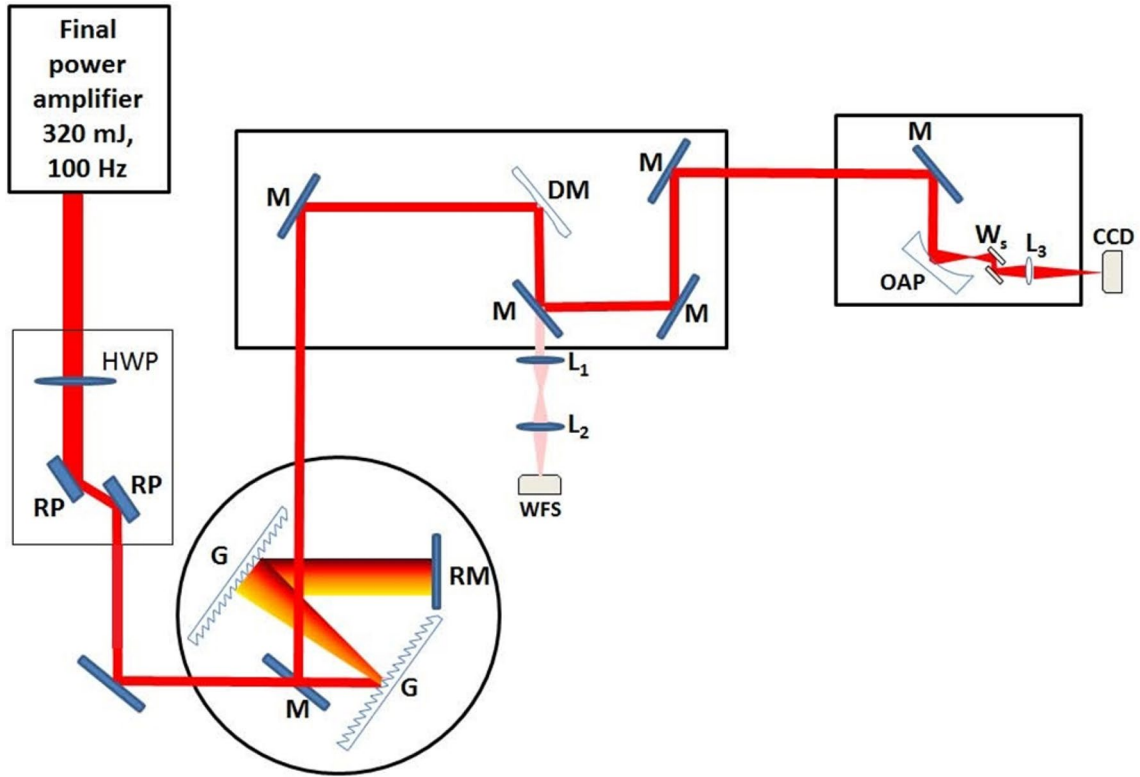


**Fig. 4** Experimental set-up for high-intensity experiments. It is made of an energy attenuator, the compressor chamber, the adaptive optics chamber and the interaction chamber. The propagation of the laser beam is represented by the red line. *HWP* half-waveplate, *RP* Brewster cut reflective polarizer, *G* diffraction grating, *RM* roof mirror, *M* dielectric coating mirror  $R_{\max}$  in 750–850 nm spectral range, *DM*

deformable mirror, *OAP* off-axis (90°) parabolic mirror (focal length of 150 mm), *WFS* wavefront sensor, *CCD* beam analyzer, *Ws* parallel planar optical window, *L1* achromatic doublet lens  $f=400$  mm, *L2* achromatic doublet lens  $f=35$  mm, *L3* achromatic doublet lens  $f=50$  mm

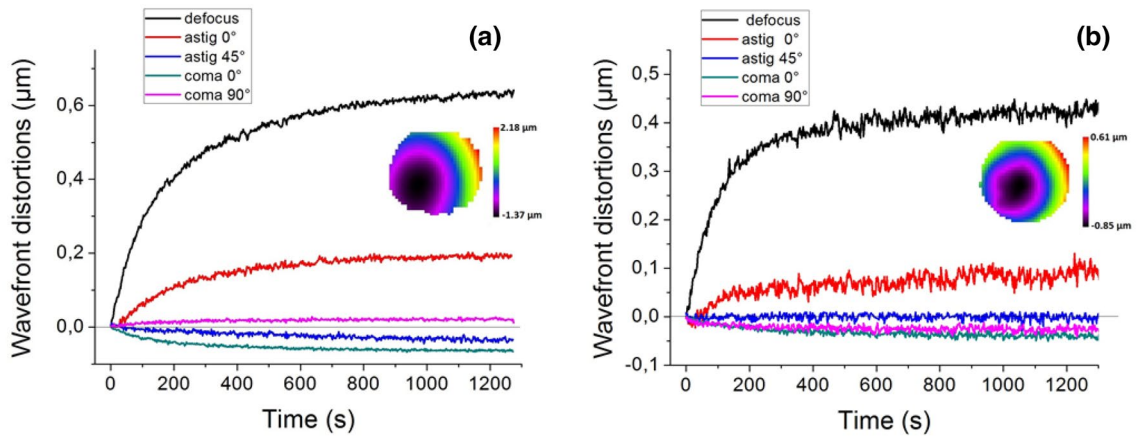


**Fig. 5** Time-dependent evolution of the Zernike polynomial coefficients for an average power of 32 W before compressor (pulse energy of 320 mJ) with the deformable mirror (a) and with a dielectric

coated mirror instead of the deformable mirror (b). In both figures, the inset shows the final wavefront measured after 1270s (~21 min) of laser operation

are indeed representative of the low-frequency aberrations of the wavefront of high average power femtosecond laser systems [12]. For instance, in this reference, it was

concluded on the primary importance of defocus, which is in agreement with our evaluation of the wavefront aberrations shown on Fig. 5.

For an average power of 32 W before compressor (320 mJ per pulse), the evolution of the low-order Zernike polynomial coefficients are plotted in Fig. 5a, b. In order to identify the respective influence of the compressor diffraction gratings and of the deformable mirror, we removed the deformable mirror and replaced it by a mirror with dielectric coating ( $R > 99.9\%$  in the 750–850 nm spectral range). Note that in this study, we consider the thermally induced distortions associated with the compressor as a whole, without analyzing separately the influence of each compressor grating.

After an operating time of approximately 800 s, all the aberration components are entering in a stationary regime (see Fig. 5) which corresponds to reaching thermal equilibrium between laser-induced heating and residual heat dissipation by the optical elements of the laser chain. Moreover, we clearly attribute these wavefront distortions to both the compressor and the deformable mirror system. Indeed, as the energy attenuation system is implemented after the last power amplifier, the latter is constantly operated at maximum average power ( $\sim 32$  W). As we do not detect any aberrations at low average power (see the 3 W case in Fig. 6), we can conclude that the only optical elements able to induce significant aberrations are located in the compression chamber and/or the adaptive optics chamber. The laser compressor is made of gratings and dielectric mirrors. We rule out the influence of the dielectric mirrors because of extremely low absorption of their coatings ( $R > 99.9\%$  over 750–850 nm bandwidth). Moreover, some of them are implemented for beam transport in the power amplifier working at the nominal average power of 32 W and it has been shown that the latter was not inducing any wavefront aberrations. So these observations allow us to conclude that

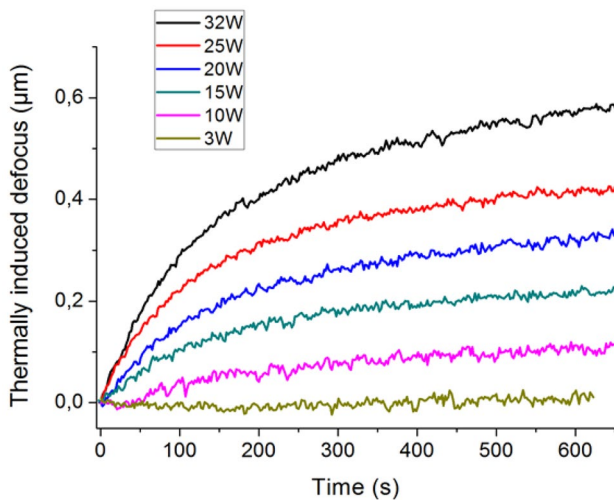


**Fig. 6** Time-dependent thermally induced defocus for different average powers before the compressor. Note that the configuration studied includes the deformable mirror (whole laser chain)

the optical elements responsible for the degradation of the wavefront at high average power are the gratings of the compressor and also the deformable mirror because the amount of wavefront distortions is slightly higher when these both elements are considered (compare Fig. 5a, b). As a similar coating (protected silver coating) is used for the OAP located in the interaction chamber, we presume also of the importance of this optics in our operating conditions.

According to Fig. 5a, b, the wavefront distortions are primarily composed of the two low-order Zernike polynomials, defocus and astigmatism at  $0^\circ$ . Figure 5a, b also shows that the diffraction gratings of the compressor are responsible for the main part of the thermally induced aberrations: for instance, after 20 min of operation, the defocus coefficient reaches 420 nm without the deformable mirror while it reaches 630 nm with the deformable mirror. The diffraction gratings (Horiba Jobin–Yvon, 1480 grooves/mm,  $65^\circ$  incidence angle) are based on a low expansion glass substrate (zerodur) with an Au reflective coating deposited on top of a resin layer. The reflection efficiency of the gratings in the zero and  $-1$  diffraction order is measured at 1 and 91% per pass respectively, which means that at maximum 8% of the initial incoming power is absorbed by the diffraction gratings. In our 4-pass Treacy type compressor, a maximum of 27.5% of the incoming pulse energy is thereby absorbed by the diffraction gratings. The deformable mirror is working at  $45^\circ$  incidence and has a protected silver coating deposited on a membrane whose composition is not specified by the manufacturer. The reflection efficiency of the mirror is measured at 93%. We consider that at maximum the remaining 7% are absorbed by the deformable mirror. So a higher amount of absorbed energy needs to be dissipated in the compressor (27.5%) as compared with the absorbed energy to be dissipated in the deformable mirror (7%) which supports the observation that the compression gratings are the main contributing elements to the wavefront distortions. Note, however, that the saturation is reached more rapidly when only the diffraction gratings are considered (compare the slopes before the saturation in Fig. 5a, b), thus suggesting that the rate of thermal dissipation is more efficient for the gratings.

We also point out the absence of thermally induced astigmatism ( $90^\circ$ ) without the deformable mirror which indicates that the negative value of the astigmatism ( $90^\circ$ ) in Fig. 5a is caused by the deformable mirror. Moreover, the coma ( $90^\circ$ ) induced by the compressor gratings and the deformable mirror (Fig. 5a) has a different sign than the one induced by the compressor gratings only (Fig. 5b). We should also note that using a DM with a dielectric coating with reflectivity close to 100% would reduce the thermal load on the DM to an insignificant level.

We now focus on the evolution of the defocus, the most important thermally induced aberration in our laser system,

as a function of the average power incoming on the compressor gratings (see Fig. 6). Note that similar qualitative behavior was observed for the other Zernike coefficients relevant to this study. We notice that the defocus aberration starts to be significant from an average power of 10 W (100 mJ per pulse at 100 Hz in our case). Indeed, for 10 W average power before the compressor, the Zernike polynomial coefficient corresponding to defocus exceeds  $\lambda/10$  (80 nm).

For average powers above 10 W before the compressor, the compressor gratings and the deformable mirror are responsible for the development of significant low-frequency thermally induced aberrations. At the maximum average power before compression (32 W @ 100 Hz) and approximately 20 min after turning the system on, we observed the saturation of the thermally induced distortions (Fig. 5a). At lower average power, the saturation is reached much earlier (see Fig. 6). For instance, this time is equal to  $\sim 600$  s (10 min) for 15 W average power.

In order to improve the laser operability and its quality of focusing, we now investigate the capability of the deformable mirror itself to compensate the development of these thermally induced aberrations.

When the beam energy is increased above 100 mJ per pulse (10 W average power), large wavefront distortions are indeed detected leading to changes of the beam profile in the focal plane. They are of different amplitude and inertia depending on the average power at which the laser is operated. However, their characteristics are fully known from our previous analysis making easy their pre-compensation with the deformable mirror through appropriate adjustment of the latter. We then block the beam

with the mechanical shutter SH1, and we wait for several minutes for allowing the heat on the different optical components to be fully dissipated and the complete system to return at its initial rest state. We then open again the shutter SH1 and we let the amplified beam propagating in the whole laser chain to observe the progressive evolution of the beam wavefront as a function of time. This is described in Fig. 7a showing the evolution of the differential wavefront distortions (peak-to-valley and RMS) corresponding to the subtraction of the actual measured wavefront to the wavefront reference which was determined beforehand when the laser was attenuated to a low average power (3 W). For further characterization in view of the development of high-intensity experiments, we also evaluate the peak intensity at the focus of the off-axis parabola (see Fig. 7b). We built a home-made code which takes into account the real 2D spatial profile of the beam at the focal point, the pulse energy on target and the pulse duration (measured in Fig. 2). For that calculation, we neglect any spatio-temporal coupling of the beam. We consider the losses induced by the compressor (31%), the deformable mirror and the parabolic mirror coatings ( $\sim 7\%$  each): the maximum pulse energy at the focal plane is 190 mJ. Moreover, to perform this measurement at high incident energy, the distance between the two gratings of the compressor is varied to significantly increase the pulse duration ( $> 1$  ps) in order to reduce the peak intensity. Indeed, when working at full energy and at the shortest pulse duration, it was observed that the beam propagating through the first optical window (Ws) was intense enough to induce an irreversible damage of

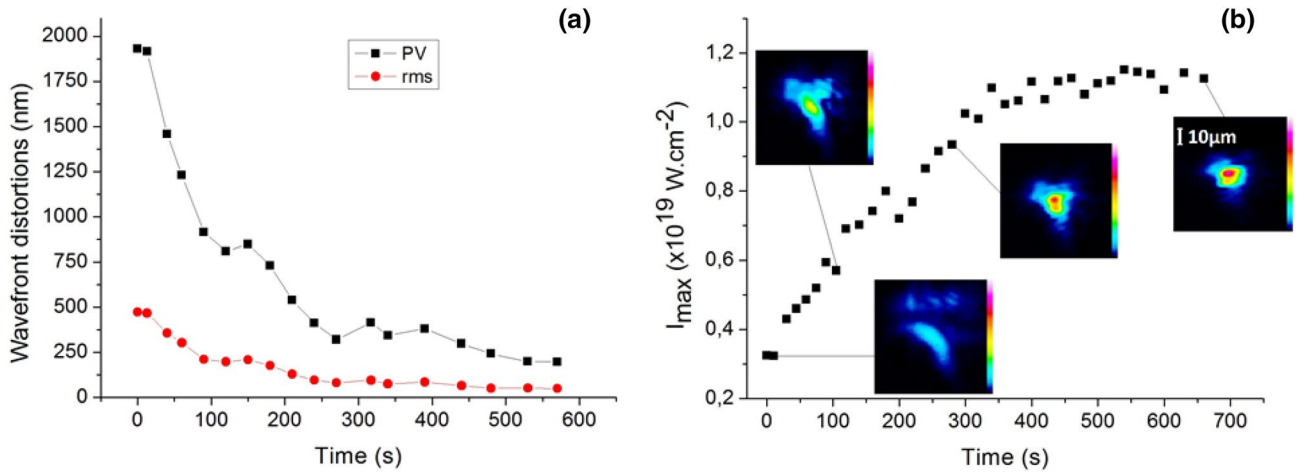


**Fig. 7** **a** Evolution of the differential beam wavefront measured at high energy (320 mJ per pulse) as compared with the wavefront measured at low energy ( $< 30$  mJ per pulse) after pre-compensation of the thermally induced wavefront distortions. **b** Evolution of the peak intensity delivered on target as a function of time. Snapshots of the beam profile in the focal plane are displayed to show the cor-

responding evolution of the beam intensity distribution in the focal plane of the parabola. A linear colormap on the side of each 2D beam profile is used to assess the beam intensity distribution. No more evolution of the peak intensity is observed after around 360 s (36,000 shots), demonstrating the successful pre-compensation of the thermally induced wavefront distortions

the substrate. Significantly decreasing the peak intensity enables to record the real beam profile without damaging Ws, even at the maximum available energy. Note that the thermally induced wavefront distortions analyzed in the current study are primarily affected by the high average power and not by the high peak intensity of the beam.

Just after opening the shutter, the differential wavefront is important [higher than  $2\lambda$  (PV) and higher than  $\lambda/2$  (rms)] because of the choice to pre-compensate the thermally induced distortions corresponding to those reached in the stationary regime when the system is fully thermalized. After around 300 s of operation, the wavefront distortions are reduced to a residual level below  $\lambda/3$  (PV) and  $\lambda/10$  (RMS) (see Fig. 7a). After around 500 s, the wavefront distortions reach a steady state to a final value around  $\lambda/4$  (PV) and  $\lambda/16$  (RMS) which corresponds to a calculated Strehl ratio of 0.85.

Figure 7b shows the corresponding evolution of the peak intensity available on target in the conditions when static pre-compensation strategy is used. At the beginning of the operation, the focal spot is distorted as the time-dependent thermal aberrations have not reached their final value corresponding to the stationary regime in the laser chain. After running the system for more than 6 min (36,000 laser shots), the beam profile no longer significantly evolves. In this steady-state regime, the beam radius is 5.3  $\mu\text{m}$  in the vertical plane and 7.6  $\mu\text{m}$  in the horizontal plane (@  $1/e^2$ ) which is around twice the diffraction limit size in the vertical axis, and three times in the horizontal axis. This is slightly larger and more asymmetric than the one measured at low power (5.1  $\mu\text{m}$  in the vertical plane and 5.3  $\mu\text{m}$  in the horizontal plane). We believe that this difference could be explained by the occurrence of thermal aberrations induced by the protected silver coating of the focusing parabolic mirror, which are not taken into account in the current study as this optics is located downstream of the wavefront sensor. Further studies needs to be performed to compensate for the wavefront distortions induced by the high thermal load on the parabolic mirror.

Finally, in the conditions corresponding to the stationary regime, approximately after 6 min operation for our laser system, we demonstrate that our strategy of pre-compensation allows us to provide a stable 100 Hz train of pulses with a peak intensity higher than  $1.1 \times 10^{19} \text{ W/cm}^2$  on target. The average displacement of the beam centroid was less than 700 nm over 100 shots, corresponding to a beam pointing stability of 10  $\mu\text{rad}$ . Note that the period of 6 min could be considerably shortened by using different strategy of pre-compensation of the thermally induced wavefront aberrations, for instance by applying a dynamic adaptive loop correction. However, such strategy is currently out of reach of our adaptive correction system.

## 4 Conclusion

We report the characterization of a high average power ( $> 22 \text{ W}$  after compression), high peak power ( $> 9.5 \text{ TW}$ ) laser chain with an ASE intensity contrast ratio of  $10^{10}$  at 100 Hz repetition rate. We studied the thermal distortions of the laser wavefront induced under high power load ( $P > 10 \text{ W}$ ) applied to the compressor diffraction gratings and to the deformable mirror. The deformable mirror enables the compensation of the thermal distortions, as they are mostly made of low-frequency aberrations. A few minutes after operating the laser at full power, the thermally induced wavefront distortions reach a steady state and the applied correction technique based on static pre-compensation of the wavefront aberrations provides 100 Hz laser femtosecond operation with stable pulse performances, namely a peak intensity above  $10^{19} \text{ W/cm}^2$  and an average power around 19 W on target which correspond to the best actual standards worldwide combining simultaneously high repetition rate ( $> 10 \text{ Hz}$ ) and high peak intensity ( $> 10^{19} \text{ W/cm}^2$ ).

In the near future, we intend to study the wavefront distortions induced by the high thermal load on the focusing parabolic mirror which are not analyzed in the current study. We also plan to study the spatio-temporal coupling of the beam potentially induced under high average power operation, which was neglected in the present study. Such a system paves the way to the study of relativistic optics at high repetition rate using moderate  $f$ -number focusing optics. Currently, it is used for the generation of sub-picosecond hard X-ray  $\text{K}_\alpha$  sources at 100 Hz.

**Acknowledgements** The research leading to these results has received funding from LASERLAB-EUROPE (grant agreement no. 654148, European Union's Horizon 2020 research and innovation programme). The financial support of European Community, Ministry of Research and High Education, Region Provence-Alpes-Côte d'Azur, Department of Bouches-du-Rhône, City of Marseille, CNRS, and Aix-Marseille University is gratefully acknowledged for funding ASUR platform.

## References

1. E. Esarey, C.B. Shroeder, W.P. Leemans, "Physics of laser driven plasma based electron accelerators. *Rev. Mod. Phys.* **81**, 1229–1285 (2009)
2. A. Macchi, M. Borghesi, M. Passoni, Ion acceleration by super-intense laser-plasma interaction. *Rev. Mod. Phys.* **85**, 751–793 (2013)
3. S. Corde, K. Ta Phuoc, G. Lambert, R. Fitour, V. Malka, A. Rousse, Femtosecond X rays from laser-plasma accelerators. *Rev. Mod. Phys.* **85**, 1–48 (2013)
4. H. Fattahi et al., Third generation femtosecond technology. *Optica* **1**(1), 45–63 (2014)
5. W.S. Brocklesby, Progress in high average power ultrafast lasers. *Eur. Phys. J.* **224**, 2529–2543 (2015)

6. F. Böhle, M. Kretschma, A. Jullien, T. Nagy, Compression of CEP-stable multi-mJ laser pulses down to 4 fs in long hollow fibers. *Las. Phys. Lett.* **9**, 095401 (2014)
7. I. Matsushima, H. Yashiro, T. Tomie, 10 KHz 40W Ti:Sapphire regenerative amplifier. *Opt. Lett.* **31**, 2066–2068 (2006)
8. S. Hädrich, M. Kienel, M. Müller, A. Klenke, J. Rothhardt, R. Klas, T. Gottschall, T. Eidam, A. Drozdy, P. Jojart, Z. Varallyay, E. Cormier, K. Osvay, A. Tünnermann, J. Limpert, Energetic sub-2-cycle laser with 216 W average power. *Opt. Lett.* **41**(18), 4332–4335 (2016)
9. G. Mourou, B. Brocklesby, T. Tajima, J. Limpert, The future is fibre accelerators. *Nat. Photon.* **7**, 258–261 (2013)
10. S. Breitkopf, T. Eidam, A. Klenke, L. Von Grafenstein, H. Carstens, S. Holzberger, E. Fill, T. Schreiber, F. Krausz, A. Tünnermann, I. Pupeza, J. Limpert, A concept for multiterawatt fibre lasers based on coherent pulse stacking in passive cavities. *Light Sci. Appl.*, **3**, e211 (2014)
11. M. Kienel, A. Klenke, T. Eidam, S. Hadrlich, J. Limpert, A. Tünnermann, Energy scaling of femtosecond amplifiers using actively controlled divided-pulse amplification. *Opt. Lett.* **39**(4), 1049–1052 (2014)
12. R. Budriunas, T. Stranislaukas, J. Adamonis, A. Aleknavicius, G. Veitas, D. Gadonas, S. Balickas, A. Michailovas, A. Varanavicius, 53W average power CEP-stabilized OPCPA system delivering 5.5 TW few cycle pulses at 1 KHz repetition rate. *Opt. Exp.* **25**(5), 5797–5806 (2017)
13. A. Vaupel, N. Bodnar, B. Webb, L. Shah, M. Richardson, Concepts, performance review, and prospects of table-top, few-cycle optical parametric chirped-pulse amplification. *Opt. Eng.* **53**(5), 051507 (2014)
14. P. Sikocinski, O. Novak, M. Smrz, J. Pilar, V. Jambunathan, H. Jelinkova, A. Endo, A. Lucianetti, T. Mocek, Time-resolved measurement of thermally-induced aberrations in a cryogenically cooled Yb–YAG slab with a wavefront sensor. *Appl. Phys. B* **73**, 122 (2016)
15. O. Slezak, A. Lucianetti, M. Divoky, M. Sawicka, T. Mocek, Optimization of wavefront distortions and thermal-stress induced birefringence in a cryogenically-cooled multislabs laser amplifier. *IEEE J. Quant. Electron.* **49**, 11 (2013)
16. M. Chyla, S.S. Nagisetty, P. Severova, T. Miura, K. Mann, A. Endo, T. Mocek, Time-resolved deformation measurement of Yb:YAG thin disk using wavefront sensor. *Proc. SPIE* **9343**, 93431E-1, (2015)
17. Y. Zhang, J. Wang, X. Lu, W. Huang, X. Li Research and control of thermal effect in a gas-cooled multislabs Nd:glass laser amplifier. *Proc. SPIE* **9621**, 962103-1, (2015)
18. C.G. Durfee, S. Backus, M.M. Murnane, H.C. Kapteyn, Design and implementation of a TW-class high average power laser system. *IEEE J. Sel. Top. Quant. Electron.* **4**, 2 (1998)
19. S. Ito, H. Ishikawa, T. Miura, K. Takasago, A. Endo, K. Torizuka, Seven terawatt Ti:sapphire laser system operating at 50 Hz with high beam quality for laser Compton femtosecond X-ray generation. *Appl. Phys. B* **76**, 497–503 (2003)
20. R.S. Nagymihaly, H. Cao, D. Papp, G. Hajas, M. Kalashnikov, K. Osvay, V. Chvykov, Liquid-cooled Ti:Sapphire Thin disk amplifiers for high average power 100-TW systems. *Opt. Exp.* **25**, 6664–6677 (2017)
21. W. Koehner, *Solid State Laser Engineering*, 6th edn. Springer, New-York (2006)
22. Y. Ning, Q. Sun, H. Wang, W. Wu, S. Du, X. Xu, Thermal distortion real-time detection and correction of a high-power laser beam-splitter mirror based on double Shack–Hartmann wavefront sensors. *Proc. SPIE* **9513**, 95130Y-1, (2015)
23. S. Fourmaux, C. Serbanescu, L. Lecherbourg, S. Payeur, F. Martin, J.C. Kieffer, Investigation of the thermally-induced laser beam distortion associated with vacuum compressor gratings in high energy and high average power femtosecond laser systems. *Opt. Exp.* **17**(1), 178–184 (2009)
24. S. Backus, R. Bartels, S. Thompson, R. Dollinger, H.C. Kapteyn, M.M. Murnane, High efficiency, single stage 7-kHz high-average-power ultrafast laser system. *Opt. Lett.* **26**(7), 465–467 (2001)
25. D.A. Alessi, P.A. Rosso, H.T. Nguyen, M.D. Aasen, J.A. Britten, C. Haefner, Active cooling of pulse compression diffraction gratings for high energy, high average power ultrafast laser. *Opt. Exp.* **24**(26), 30015–30023 (2016)
26. D.M. Gaudiosi, A.L. Lytle, P. Kohl, M.M. Murnane, H.C. Kapteyn, S. Backus, 11-W average power Ti:sapphire amplifier system using downchirped pulse amplification. *Opt. Lett.* **29**(22), 2665–2667 (2004)
27. J. Itatani, J. Faure, M. Nantel, G. Mourou, S. Watanabe, Suppression of the amplified spontaneous emission in chirped-pulse-amplification lasers by clean high-energy seed-pulse injection. *Opt. Commun.* **148**(1–3), 70–74 (1998)
28. G. Chériaux, P. Rousseau, F. Salin, J.P. Chambaret, B. Walker, L.F. Dimauro, Aberration-free stretcher design for ultrashort-pulse amplification. *Opt. Lett.* **21**(6), 414–416 (1996)
29. F. Verluise, V. Laude, Z. Cheng, C. Spielmann, P. Tournois, Amplitude and phase control of ultrashort pulses by use of an acousto-optic programmable dispersive filter: pulse compression and shaping. *Opt. Lett.* **25**, 575–578 (2000)
30. T. Oksenhendler, D. Kaplan, P. Tournois, G.M. Greetham, F. Estable, Intracavity acousto-optic programmable gain control for ultra-wide-band regenerative amplifier. *Appl. Phys. B* **83**, 491–495 (2006)
31. M. Pittman, S. Ferré, J.P. Rousseau, L. Notebaert, J.P. Chambaret, G. Chériaux, Design and characterization of a near diffraction-limited fs 100 TW 10 Hz high intensity laser system. *Appl. Phys. B* **74**, 529–535 (2002). <https://doi.org/10.1007/s00340-010-3916-y>
32. T. Oksenhendler, S. Coudreau, N. Forget, V. Crozatier, S. Gabrielle, R. Herzog, O. Gobert, D. Kaplan, Self-referenced spectral interferometry. *Appl. Phys. B* **99**, 7–12 (2010). <https://doi.org/10.1007/s00340-010-3916-y>
33. Y. Azamoum, V. Tcheremiskine, R. Clady, A. Ferré, L. Charmasson, O. Uteza, M. Sentis, Impact of the pulse contrast ratio on molybdenum  $K_{\alpha}$  generation by ultrahigh intensity femtosecond laser solid interaction. *Sci. Rep.* **8**, 4119 (2018)
34. S. Fourmaux, S. Payeur, S. Buffechoux, P. Lassonde, C. St-Pierre, F. Martin, J.C. Kieffer, Pedestal cleaning for high laser pulse contrast ratio with a 100 TW class laser system. *Opt. Exp.* **19**(9), 8486–8497 (2011)
35. N.V. Didenko, A.V. Konyashchenko, A.P. Lutsenko, S.Y. Tenyakov, Contrast degradation in a chirped-pulse amplifier due to generation of prepulses by postpulses. *Opt. Exp.* **16**, 53178–53190 (2008)
36. D.N. Schimpf, E. Seise, J. Limpert, A. Tünnermann, The impact of spectral modulations on the contrast of pulses of nonlinear chirped-pulse amplification systems. *Opt. Exp.* **16**(14), 10664–10674 (2008)
37. G. Doumy, F. Quéré, O. Gobert, M. Perdrix, P. Martin, P. Audebert, J.C. Gauthier, J.P. Geindre, T. Wittmann, Complete characterization of a plasma mirror for the production of high contrast ultraintense laser pulses. *Phys. Rev. E* **69**, 026402 (2004)
38. N. Lefaudeux, E. Lavergne, S. Monchoce, X. Levecq, Diffraction limited focal spot in the interaction chamber using phase retrieval adaptive optics. *Proc SPIE*, **8960**, 89601R (2014)
39. M. Born, E. Wolf, *Principles of Optics*, Sec. 9.2 (Pergamon, New York, 1975)
40. J.Y. Wang, D.E. Silva, Wave-front interpretation with Zernike polynomials. *Appl. Opt.* **19**(9), 1510 (1980)